The Light Features and Bredigite Layout for Orthosilicate Phosphor in WLED Devices

My Hanh Nguyen Thi[1], Nguyen Le Thai[2], Thuc Minh Bui[3], Sang Dang Ho[4*]

[1]*Faculty of Mechanical Engineering, Industrial University of Ho Chi Minh City, Ho Chi Minh City, Vietnam*
[2]*Faculty of Engineering and Technology, Nguyen Tat Thanh University, Ho Chi Minh City, Vietnam*
[3]*Faculty of Electrical and Electronics Engineering, Nha Trang University, Nha Trang City, Vietnam*
[4]*Faculty of Electrical and Electronics Engineering, Ton Duc Thang University, Ho Chi Minh City, Vietnam*

Abstract. We created a green phosphor $Ca_{14-x}Eu_xMg_2[SiO_4]_8$ or CMS:Eu^{2+} to be utilized in WLED devices. The phosphor offers a wide spectrum achieving the highest value of 505 nm when excited at 400 nm, as a result of a shift between the excited state of $4f^65d$ and the ground state of $4f^7$ in an ion of Eu^{2+}. The interactivity of dipole-dipole appeared to be a primary power shift for the electrical multipolar nature of the phosphor. We acquired a critical distance measured at 12.9 Å as well as 14.9 Å via a critical Eu^{2+} concentration as well as the Dexter hypothesis on power shift. Via an encapsulant, we combined CMS:Eu^{2+} as well as a phosphor in red with a LED device having a λ_{max} value of 395 nm and managed to acquire white illumination having a CRI value measured at 91 at a 20-milliampere forward bias current. In addition, we also examined the layout as well as the light features in CMS:Eu^{2+}.

Keywords: Color homogeneity; Double-layer phosphor; Luminous flux; Monte Carlo theory; WLEDs

1. Introduction

WLED devices have become increasingly common due to their many advantages which include small power drain, high durability, high performance, etc (Alexeev *et al.*, 2021; Chang *et al.*, 2021; Bindai, Annapurna, and Tarafder, 2019). On the other hand, these devices still have certain limitations that prevent them from becoming standard optical devices. It is possible to create white illumination via daubing yellow phosphor on blue chips of LED. Such a procedure may yield a significant lumen exceeding 30 lm/W. On the other hand, it results in low CRI below 65, which is caused by a faint red discharge (Huu and Thi, 2022; Hakim *et al.*, 2021). It is worth noting that the majority of phosphors do not possess an absorption line between 440 nm and 460 nm. This downside is not present in the yellow phosphor $Y_3Al_5O_{12}$:Ce^{3+} or YAG:Ce^{3+} (Chen *et al.*, 2020). Therefore, the industry has managed to a novel WLED form that offers desirable features of hue generation. Many novel phosphors have been created for WLED, such as oxide, oxyfluoride, nitride, oxynitride host latticework, etc (Hsin *et al.*, 2021; Jain *et al.*, 2020) subjected to non-ultraviolet light. While these phosphors have proved to be promising, we would still need further research for the task of eliminating certain problems to achieve strong performance, superior heat

consistency, as well as improvement in hue features. When it comes to WLED devices, The best options would be alkaline-earth silicate phosphors as they offer great performance as well as heat and chemical reliability. Some mixtures were acknowledged and proposed, which have a universal structure of Sr_2SiO_4 that crystallizes within the tetragonal space group Pmnb (S. G. No. 62). With this taken into account, our investigation focused on $Ca_{14}Mg_2[SiO_4]_8$ (CMS, S. G. No. 34, Pnn2) - a bregidite mineral. The earliest examination concerning the powder X-ray data for CMS on the basis of a novel pinwheel setting was done by Araki and his colleagues. According to Sun *et al.* (2022), α-Ca_2SiO_4 along with Bredigite appeared to be distinctive phases. Li *et al.* (2020) claimed that β-Ca_2SiO_4 appeared to be based on $K_2[SO_4]$.

The space group pedigree of bredigite results in *Pmnn* → *Pnn2*, caused by the tetrahedral's leaning. This would decrease the symmetrical mechanic to *Pnn2* (Ma *et al.*, 2021; Qin, Shi, and Leon, 2020).

Our investigation focuses on the layout as well as light features of the phosphor CMS:Eu^{2+}. Specifically, the investigation concerns the power shift of Eu^{2+} with critical concentration as well as Dexter's hypothesis on power shift. We constructed a WLED device by creating a merger between an InGaN chip of LED with λ_{max} value of 395 nm and CMS:Eu^{2+}. Furthermore, we also examined the heat abatement for the luminescence and compared the mechanism in the phosphor Sr_2SiO_4.

2.   Computational Simulation

2.1. Preparation of green-emitting $Ca_{14-x}Eu_xMg_2[SiO4]_8$ (CMS:Eu^{2+}) phosphor

Table 1 The constituents and preparation of CMS:Eu^{2+}

Materials	Purity	Preparation
$CaCO_3$	99.99%	Grind the materials altogether and heat the mixture between 1100^oC and 1400^oC under a lowering atmosphere containing H_2/N_2 (5%/95%) for four hours
MgO	99.9%	
SiO_2	99.9%	
Eu_2O_3	99.99%	

Table 2 The characteristics of CMS:Eu^{2+}

Characteristics	Examination Methods
Powder X-ray diffraction (XRD)	Cu-Kα radiation under an angle of $10^o \leq 2\theta \leq 100^o$ having 0.026^o step size
Crystal layout purification	Rietveld technique
Photoluminescence under room temperature	Hitachi F-4500 luminescence spectrophotometer scanning a wavelength limit between 300 nm and 700 nm
Quantum performance	Quantum performance assessment system under excitation of 400 nm
Diffuse reflectance absorption spectra	Varian Cary 500 Scan UV-visible-NIR spectrophotometer under wavelength limit between 200 nm and 600 nm

We created the LED device via daubing an InGaN LED with a compound containing CMS:Eu^{2+}, a phosphor in red and translucent resin. The electroluminescence was determined by putting a separate LED constructed above *m*-plane GaN on silver headers linked with golden wires to work under electricity. Afterward, we covered the LED with a compound of phosphor and silicone. The compound was put above the headers and cured. Once the preparation was finished, we set the LED for assessment within a sphere with DC

bias forward states. The unit cell for CMS appears to be a structured mixture of Ca:Mg that possesses a desirable polyhedral layout of $X^{[12]}X_2^{[9]}Y^{[10]}M^{[6]}[TO_4]_4$ with X and Y being the huge polyhedral, M being the octahedron with T being tetrahedron. The desirable upper restriction for Mg presence in bredigite would be $Ca_{14}Mg_2[SiO_4]_8$. For the layout of bredigite, the MgO_6 octahedra bond through the tetrahedra to create bindings traveling parallel to the axis of α. For the layout, Ca would settle in the locations of $2a$ and $4c$, Mg would settle in the location of $2b$, while Si and O would settle in the location of $4c$. The eight locations of Ca would be related to polyhedral having 9-, 10-, and 12- coordination. These locations would be replaced with the ions of Eu. If the ions merge with the CMS crystal layout, they could replace every cation location which includes Ca^{2+}, Mg^{2+}, and Si^{4+}. On the other hand, with the ion radius and the permitted value of oxygen coordination (n) taken into account, Ca^{2+} (1.12 Å, n value of 8), Mg^{2+} (0.72 Å, n value of 6) and Si^{4+} (0.26 Å, n value of 4), replacing the ions of Mg^{2+} as well as Si^{4+} with those of Eu^{2+} (1.25 Å, n value of 8) would be a challenging task (Shadalou, Cassarly, and Suleski, 2021; Shi *et al.*, 2021).
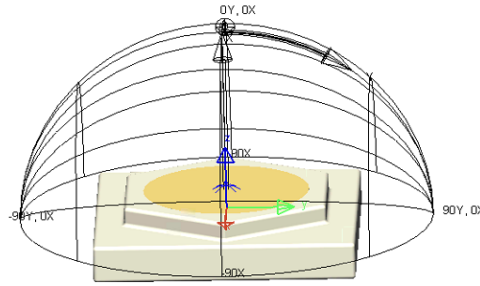

Figure 1 Photograph of WLEDs

2.2. Spectra optimization of the CCT

Figures 2(b) and 2(c) demonstrate the correlation between the apex location, intensity of discharge, and replacement of Eu^{2+}. As the concentration of Eu^{2+} rises, the discharge line with λ_{ex} value of 400 nm will move towards a greater wavelength, which is the result of the repeating absorbing activity among the ions of Eu^{2+} instead of the alterations within the crystal field surrounding Eu^{2+} which can be expressed via the following equation (Shih *et al.*, 2020):

$$\Delta = Dq = \frac{Ze^2r^4}{6R^5} \tag{1}$$

where Dq represents the crystal field of the octahedral symmetrical mechanism. R represents the range separating the center ion from its ligands. Z represents the anion's charge or valence. e represents the electron's charge. r represents the d wavefunction's radius. Therefore, the cleavage of the crystal field would not be the primary cause of the red shift because of the ion radius for Ca^{2+} with 8- coordinate being inferior to Eu^{2+} (1.12 Å and 1.25 Å). It is clear in Figure 2(c) that the optimal replacement for Eu^{2+} from CMS:Eu^{2+} would be an x value of 0.3. If this value rises, the relative intensity of discharge will occur, caused by the abatement of concentration. It is possible to assess the critical range of power shift or R_c for CMS:Eu^{2+} via the layout data containing the unit cell's volume (V), the quantity of locations of Eu^{2+} for each cell (N), as well as the critical concentration (X_c).

$$R_c \approx 2\left(\frac{3V}{4\pi X_c N}\right)^{1/3} \tag{2}$$

where R_c represents the mean splitting among the closest ions of Eu^{2+} under X_c. With a V value of 1356 Å^3, an N value of 8, and an X_c value of 0.3, the critical shift range for Eu^{2+} would be roughly 12.9 Å.
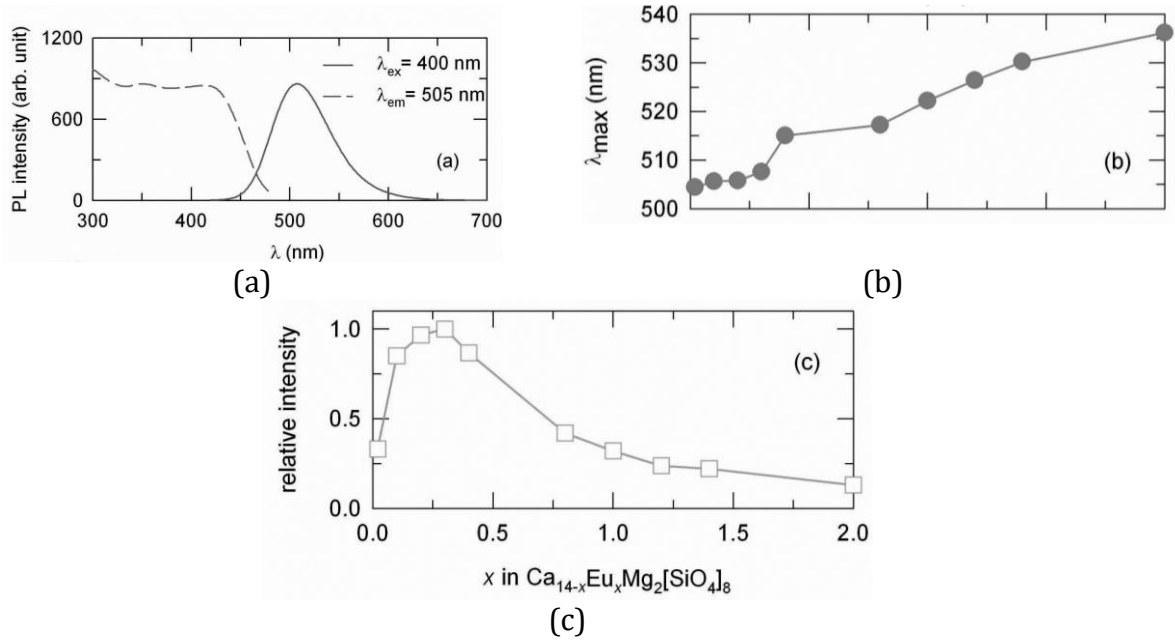
(a)

(b)

(c)

Figure 2 (a) Discharge and emission spectra in CMS:Eu^{2+} when excited at 400 nm under different concentrations of Eu^{2+} (x). (b) The location for the maximal discharge. (c) The relative intensity of discharge along with replacement of Eu^{2+} (x)

The Dexter expression was utilized to determine the shift for the electrical dipole-dipole interactivity as the symmetrical permitted shifts of Eu^{2+} are involved (Singh *et al.*, 2021). The critical range is calculated based on Blasse expression:

$$P_{SA} = \frac{2\pi}{h}|\langle S, A^*|H_{SA}|S^*, A\rangle|^2 \int g_S(E)g_A(E)dE \qquad (3)$$

$$R_c^6 = 0.63 \times 10^{28} \frac{4.8\times10^{-16}.P}{E^4} \int f_S(E)F_A(E)dE \qquad (4)$$

where P represents oscillator potency for the ion of Eu^{2+}. E represents the energy for the maximal spectrum overlay. $\int f_S(E)F_A(E)dE$ represents the outcome of normalized spectrum forms for discharge as well as excitation. From Figure 2, it is possible to acquire E as well as $\int f_S(E)F_A(E)dE$ via the spectrum information. In the case of P related to the wide absorbing line of $4f^7 \rightarrow 4f^65d$, we will acquire a 10^{-2} value [24,26]. E and $\int f_S(E)F_A(E)dE$ reach 2.66 eV and 1.88 x 10^{-2} eV^{-1}. With 4, the critical range would be 14.9 Å.

The non-radioactive power shift between two ions of Eu^{2+} could take place through reciprocity, re-absorption of radioactivity, or interactivity of multipole-multipole. According to Dexter, reciprocity causes a power shift of prohibited shift. In addition, the standard critical ranges would be roughly 5 Å [25]. Hence, reciprocity might not join the power shift among the ions of Eu^{2+}. As such, the Eu^{2+} power shift would be the permitted electric-dipole shift of $4f^7 \rightarrow 4f^65d$. Based on the hypothesis of Dexter, we ought to manage the power shift activity via electric multipole-multipole interactivity (Tian *et al.*, 2020). The following formula will determine the intensity of discharge or *I* for each trigger ion (Tuyet *et al.*, 2020):

$$\frac{I}{c} = \frac{k}{\left[1+\beta C^{\frac{\theta}{3}}\right]} \qquad (5)$$

where C represents trigger concentration that abates itself. k and β are constants corresponding to interactivity within an identical excitation state of a host's latticework. If

C >> X_c, the non-radioactive depletions could be caused by a multipolar shift. It is possible to alter the formula (5) (Wang *et al.*, 2020):

$$\frac{I}{c} = \frac{k_1}{\beta C^{\frac{\theta}{3}}} \tag{6}$$

where k_1 represents a constant. The θ values of 6, 8 and 10 corresponds to dipole-dipole, dipole-quadrupole and quadruple-quadrupole. It is possible to assess θ via the slop $-\theta/3$ from the linear dash demonstrated by Figure 3. The Figure puts log(I/C) and log(C) on a logarithmic scale. The result for $-\theta/3$ would reach -2.16, and as such, θ assumes a value of roughly 6. Such an outcome points out the dipole-dipole interactivity would be the concentration abatement activity for the discharge of Eu^{2+}. From Figure 4, we can see the diffuse reflectance absorption spectra of CMS:Eu^{2+}. It is possible to determine the Kubelka-Munk absorption coefficient (K/S) via a correlation: the absorbance (A) for CMS as well as CMS:Eu^{2+} can be assessed with the reflectances (R) via an expression (Yu *et al.*, 2021):

$$\frac{K}{S} = \frac{(1-R)^2}{2R} \tag{7}$$

Using the shown expression, the line gap power or E_g for CMS:Eu^{2+} assumed a value of 2.56 eV. From this result, it might be impossible for the excitation power for n-UV (400 nm, 45000 cm^{-1}) to shift between the valence line and conduction band. CMS does not display any absorption at below 380 nm and became white as a result. Hence, it is possible to excite the electrons of the $4f^7$ states in Eu^{2+} via n-UV illumination within the $4f^65d$ state. We determined the quantum performance via a 400-nm excitation cause. The performance reached roughly 23% under room temperature, lower than the 85% result of Sr_2SiO_4:Eu^{2+}.
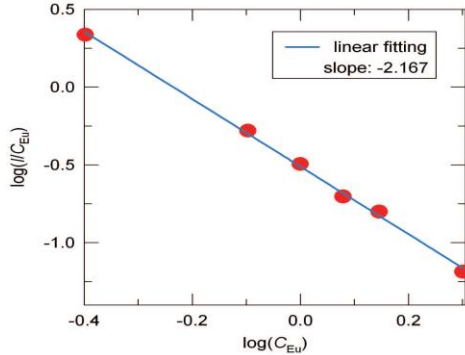

Figure 3 The logarithm for the intensity of discharge for each trigger ion (log I/CEu) along with the logarithm for the concentration of Eu^{2+} (log CEu) from CMS:Eu^{2+} with λ_{ex} value of 400 nm
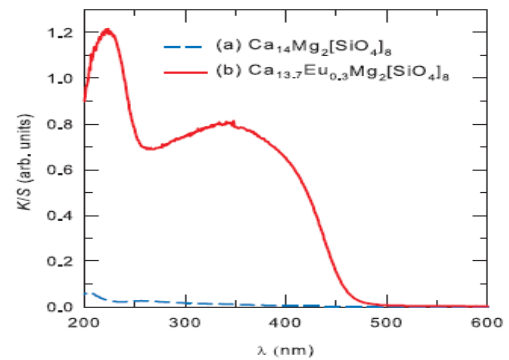
Figure 4 The diffuse reflectance spectra of (a) CMS and (b) CMS:Eu^{2+} when excited at 400 nm

Between room temperature and 150ºC, the intensities of photoluminescence in CMS:Eu^{2+} and Sr_2SiO_4:Eu^{2+} suffered a penalty of 11% and 18%, which is demonstrated by Figure 5(a). If the task is to examine the heat abatement features, we need to determine the trigger power via Arrhenius expression (Zhang *et al.*, 2020; Yuce *et al.*, 2019):

$$I(T) = \frac{I_0}{1 + A.exp\left(\frac{-E}{kT}\right)} \tag{8}$$

I_0 represents the first intensity. $I(T)$ indicates the intensity under a specific (T) temperature. A represents a constant. E represents the trigger power of heat abatement. k represents the constant of Boltzmann. In Figure 5(b), we can see $\ln[(I_0/I)-1]$ and $1/(kT)$.

Through utilizing the Arrhenius expression, the values of trigger power (E) for CMS:Eu^{2+} and Sr$_2$SiO$_4$:Eu^{2+} appeared to be 0.348 eV and 0.158 eV.

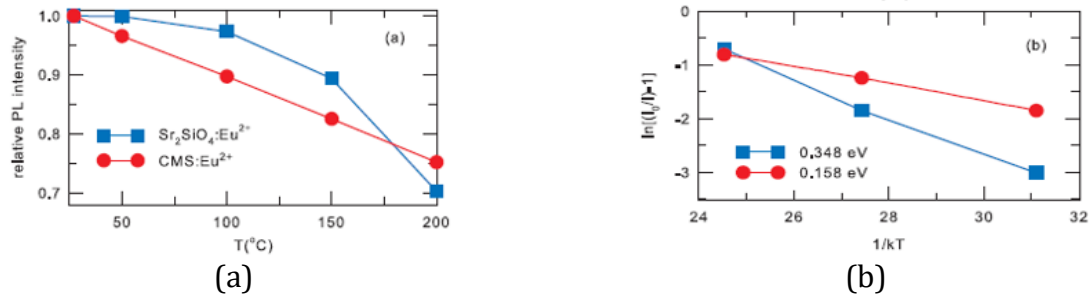(a)   (b)

Figure 5 (a) The intensities of discharge reliant on temperature. (b) The heat abatement in Sr$_2$SiO$_4$:Eu^{2+} as well as CMS:Eu^{2+} when Arrhenius expression is utilized

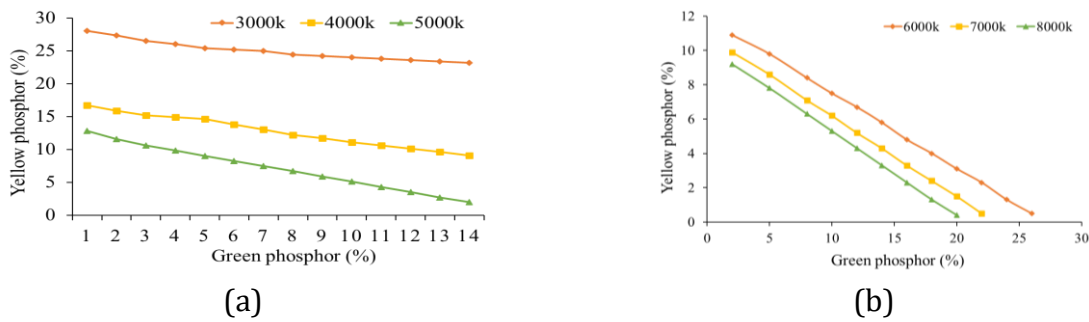(a)   (b)

Figure 6 Sustaining the median CCT level via the modification of concentration: (a) 3000 K-5000 K; (b) 6000 K-8000 K

With the use of the software LightTools 9.0 and the Monte Carlo approach, the flat phosphor sheet for a multi-chip WLED (MCW-LED) was reproduced (Zhang *et al.*, 2021). The recreation procedure would have two main phases. First, assessing as well as constructing the layout samples along with optical characteristics in MCW-LED lights. Second, managing the phosphor mixture and the light influences through many CMS:Eu^{2+} doping amount percentages. For the assessment of YAG:Ce^{3+} and CMS:Eu^{2+} compound's effects on WLED lights' performance, generating variants would be compulsory. Examining two kinds of compounds under the median CCT values of 3000 K, 4000 K, and 5000 K, a remote phosphor layout with two sheets would be necessary. Via Figure 1, the modeling illustration of the MCW-LED with a conformal phosphor structure and a great 8500 K CCT value is presented. It also reveals that the initial MCW-LEDs' recreation does not involve CMS:Eu^{2+}. The WLED components' dimensions can be listed as follows. A reflector with 2.07×8×9.85 mm for height and bottom- and top-surface length, respectively; a 0.08 mm thick film of conformal phosphor compounding would be daubed on the chips; a set of nine chips with a size of 1.14×0.15 mm (length × height) and radiant-flux value of 1.16 W, and 453 nm peak wavelength for each is attached to LED reflector's gap.

3.   Results and Discussion

Figure 6 depicts the relation between the utilizing concentration of CMS:Eu^{2+} and YAG:Ce^{3+}. In particular, it shows the inverse data trend between these two phosphor amounts: the increase (2-20%) of CMS:Eu^{2+} content leads to the decrease of YAG:Ce^{3+} content, at both 4000 K and 8000 K. This opposite serves as a median to sustain the CCT value and cause changes to either absorptivity or dispersion of light in the WLED model. As a result, we can manage to achieve the desired results for WLED illumination by modifying the CMS:Eu^{2+} concentration.
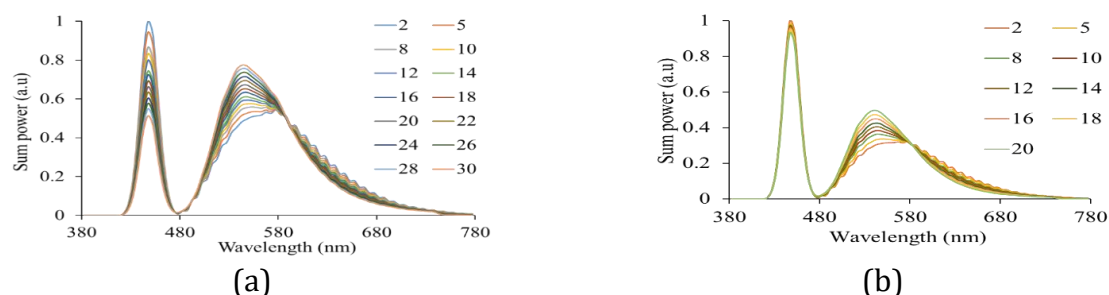
(a)   (b)

Figure 7 The emission spectra in WLED devices and the CMS:Eu^{2+} concentrations: (a) 4000 K; (b) 8000 K

Figure 7 illustrates how the concentration of green phosphor CMS:Eu^{2+} influence the emission power of the WLED at 4000 K and 8000 K, from which the producer can determine suitable CMS:Eu^{2+} concentration to apply to their LED products. If they want to get high and strong luminescence for backlight application, for example, they can allow a minor deduction in the chromatic features. As depicted in both Figures 7(a) and 7(b), two critical spectral regions for white light generation, 420-480 nm, and 500-640 nm are improved with increasing CMS:Eu^{2+} concentration, suggesting the enhancement in the luminescent output of the WLED model. Additionally, the addition of green phosphor seems to stimulate the emission and dispersion of blue light, which will contribute to increasing the possibility of blue-light conversion and extraction. Thus, the active dispersion and color consistency could be improved. This result is crucial and essential for the application of CMS:Eu^{2+} phosphor to serve the enhancement of WLED-lighting performance, especially at high CCT like 8000 K.

The discussed states can be further demonstrated with the data in Figures 8 and 9. The luminous intensity of the white light from the WLED in connection with CMS:Eu^{2+} concentration is shown in Figure 8. When the concentration of CMS:Eu^{2+} grows in the range of 2-25%, a notable rise is recorded at 5000 K – 8000 K. In Figure 9, the decreases in deviating CCT proportions decline as CMS:Eu^{2+} content becomes higher, suggesting the enhancement in CCT consistency. The green phosphor scattering and absorbing activities could be applied to explain this phenomenon. The green phosphor particles will absorb the blue illumination more significantly than the yellow illumination, as the blue emission wavelength is shorter than the yellow one. This allows greener illuminations to be generated by converting these absorbed illuminations. In other words, the green spectral component is increased as the concentration of CMS:Eu^{2+} is higher, contributing to compensating the green-light energy shortage to result in better light color consistency and luminosity.
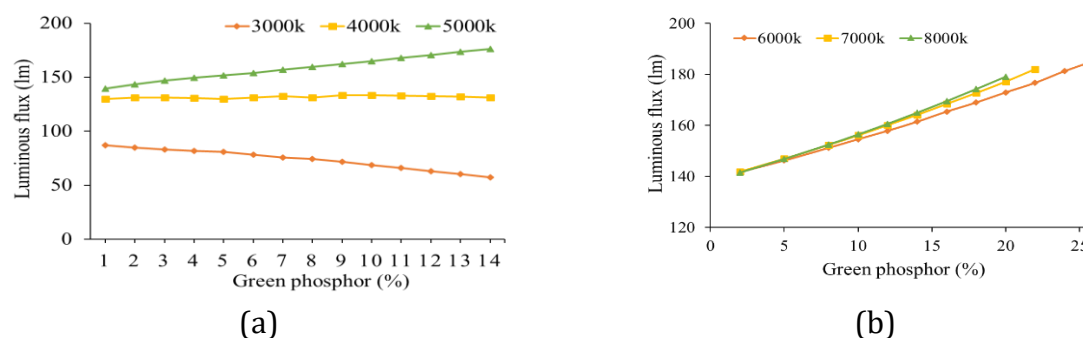

(a)   (b)

Figure 8 The lumen in the WLED devices with respective CMS:Eu^{2+} concentrations: (a) 3000 K-5000 K; (b) 6000 K-8000 K

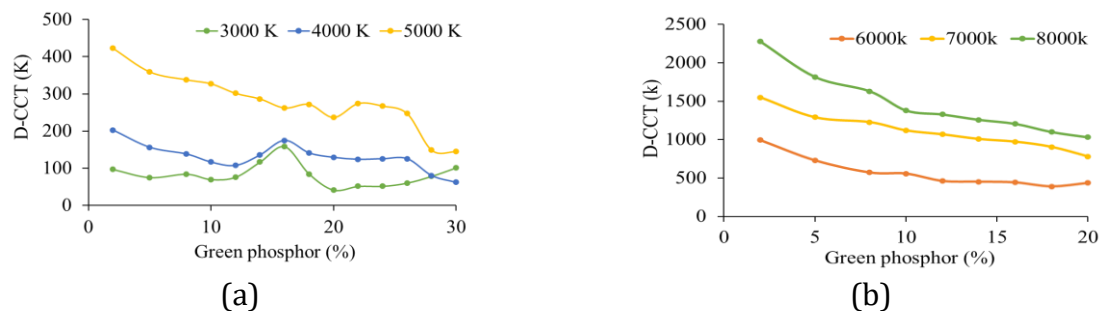(a)   (b)

Figure 9 The hue aberration in the WLED device along with CMS:Eu²⁺ concentrations: (a) 3000 K-5000 K; (b) 6000 K-8000 K

Though color uniformity is a vital and essential factor for high white-light color quality, the color rendering intent and reproduction efficiency should not be ignored. Thus, the CRI (color rendering index) and CQS (color quality scale) are subsequently examined and discussed. Figures 10 and 11 present the data of CRI and CQS, respectively. As shown, CRI values decline gradually with the surge of CMS:Eu²⁺ content percentage. Meanwhile, the CQS displays an increase with the rising concentration of CMS:Eu²⁺ within 2-10%. More than 10% CMS:Eu²⁺ obviously causes the CQS to degrade. Such events can be attributed to green-energy domination, which means the green light is generated excessively, causing the lack of other critical emission colors (blue and yellow). Therefore, the balance and homogeneity of white-light emission colors are damaged, leading to the mentioned degradation in CRI and CQS. However, the rise and stability in CQS with <10% CMS:Eu²⁺ is an important result because the CQS is more complex and difficult to control than the CRI. Specifically, managing CQS means managing to satisfy the three critical factors: color coordinates, CRI, and the observer's visual inclination. So, we should consider the optical goals to determine the suitable concentration of CMS:Eu²⁺.
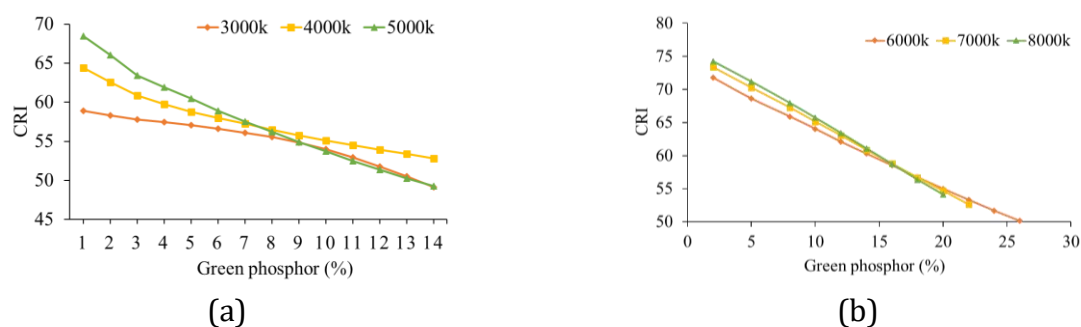

(a)   (b)

Figure 10 CRI in the WLED devices with the respective CMS:Eu²⁺ concentrations: (a) 3000 K-5000 K; (b) 6000 K-8000 K

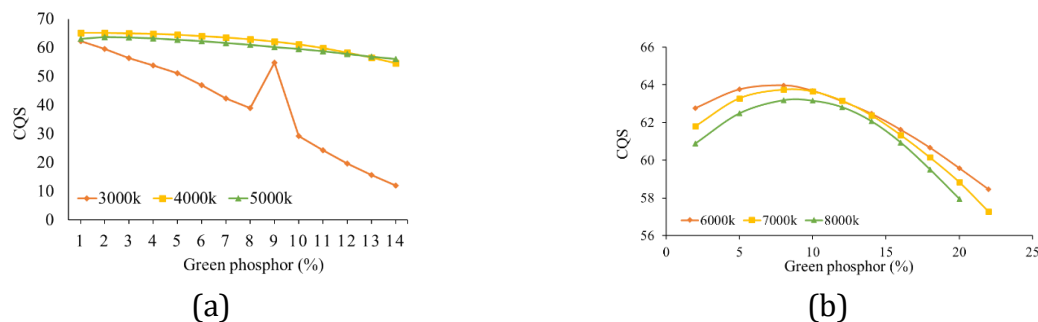(a)   (b)

Figure 11 CQS in the WLED devices with respective CMS:Eu²⁺ concentrations: (a) 3000 K-5000 K; (b) 6000 K-8000 K

4. Conclusions

Our study investigates how the green phosphor CMS:Eu^{2+} would impact the lighting features in the two-sheet phosphor layout. Judging the Monte Carlo recreations, this phosphor would be appropriate for the task of augmenting hue homogeneity, which can be applied to WLED devices possessing hue temperature measured at 5600 K and greater than 8500 K. Our study has managed to augment the hue output as well as the lumen. Achieving these elements can be fairly difficult in the case of remote phosphor layouts. On the other hand, there is a small downside to CRI as well as CQS. If the CMS:Eu^{2+} concentration rises too high, both of these elements would fall considerably. As such, choosing an appropriate concentration by considering the producer's requirements is very important. Our study can be useful data for the task of acquiring superior hue homogeneity as well as lumen in WLED devices.

Acknowledgments

References

Alexeev, A., Linnartz, J.M.G., Arulandu, K., Deng, X., 2021. Characterization of Dynamic Distortion in LED Light Output for Optical Wireless communications. *Photonics Research*, Volume 9(6), pp. 916–928

Bindai, S., Annapurna, K., Tarafder, A., 2019. Realization of Phosphor-in-Glass Thin Film on Soda-Lime Silicate Glass with Low Sintering Temperature for High Color Rendering White LEDs. *Applied Optics*, Volume 58(9), pp. 2372–2381

Chang, Y., Shih, H., Liu, C., Chen, H., Tsai, S., Li, K., Han, P., Cheng, W., 2021. Laser-Assisted LED for Adaptive-Driving-Beam Headlights Employing Ultra-Reliable Single Crystal Phosphor for Autonomous Vehicles. *Optics Express*, Volume 29(17), pp. 26466–26473

Chen, Y., Wang, J., Zhang, J., Cao, G., 2020. Light Source for Comfortable Lighting and Trapping Pests in Tea Gardens Based on Solar-Like Lighting. *Applied Optics*, Volume 59(27), pp. 8459–8464

Hakim, F.N., Muhamadinah, Y., Atthaillah, A., Mangkuto, R.A., Sudarsono, A.S., 2021. Building Envelope Design Optimization of a Hypothetical Classroom Considering Energy Consumption, Daylighting, and Thermal Comfort: Case Study in Lhokseumawe, Indonesia. *International Journal of Technology*, Volume 12(6), pp. 1217–1227

Huu, P.D., Thi, D.A.N., 2022. Selection of multi-layer remote phosphor structure for heightened chromaticity and luminous performance of white light-emitting diodes. *International Journal of Technology*, Volume 13(4), pp. 837–847

Hsin, S., Hsu, C., Chen, N., Ye, C., Ji, G., Huang, K., Hsieh, H., Wu, C., Dai, C., 2021. Design and Fabrication of A Downlight Luminaire with a Dual Frusto-Conical Reflector. *Applied Optics*, Volume 60(25), pp. 7775–7783

Jain, B., Velpula, R.T., Bui, H.Q.T., Nguyen, H.D., Lenka, T.R., Nguyen, T.K., Nguyen, H.P.T., 2020. High Performance Electron Blocking Layer-Free Ingan/Gan Nanowire White-Light-Emitting Diodes. *Optics Express*, Volume 28(1), pp. 665–675

Li, H., Li, P., Zhang, H., Chow, Y.C., Wong, M.S., Pinna, S., Klamkin, J., Speck, J.S., Nakamura, S., DenBaars, S.P., 2020. Electrically Driven, Polarized, Phosphor-Free White Semipolar (20-21) InGaN Light-Emitting Diodes Grown on Semipolar Bulk GaN Substrate. O*ptics Express*, Volume 28(9), pp. 13569–13575

Ma, L., Zhao, Y., Du, M., Pei, X., Feng, X., Sun, F., Fang, S., 2021. Phase-Error-Compensation-Based Surface Recovery Algorithm Using Spectrum Selection for White Light Interferometry. *Applied Optics*, Volume 60(21), pp. 6030–6043

Qin, L., Shi, X., Leon, A.S., 2020. Luminance Calculation Method Accounting for Mesopic Vision and Fog Penetration Ability. *Applied Optics*, Volume 59(3), pp. 683–686

Shadalou, S., Cassarly, W.J., Suleski T.J., 2021. Tunable Illumination for LED-Based Systems Using Refractive Freeform Arrays. *Optics Express*, Volume 29(22), pp. 35755–35764

Shi, L., Zhao, X., Du, P., Liu, Y., Lv, Q., Zhou, S., 2021. Enhanced Performance of Gan-Based Visible Flip-Chip Mini-LEDs With Highly Reflective Full-Angle Distributed Bragg Reflectors. *Optics Express*, Volume 29(25), pp. 42276–42286

Shih, H.K., Liu, C.N., Cheng, W.C., Cheng, W.H., 2020. High Color Rendering Index of 94 in White LEDs Employing Novel CaAlSiN3: Eu^{2+} and $Lu_3Al_5O_{12}$: Ce^{3+} Co-Doped Phosphor-in-Glass. *Optics Express*, Volume 28(19), pp. 28218–28225

Singh, K.J., Fan, X., Sadhu, A.S., Lin, C.H., Liou, F., Wu, T., Lu, Y., He, Jr., Chen, Z., Wu, T., Kuo, H., 2021. $CsPbBr_3$ Perovskite Quantum-Dot Paper Exhibiting a Highest 3 Db Bandwidth and Realizing A Flexible White-Light System for Visible-Light Communication. *Photonics Research*, Volume 9(12), pp. 2341–2350

Sun, C.C., You, A.H., Teo, L.L., 2022. XRD Measurement for Particle Size Analysis of PMMA Polymer Electrolytes with SiO_2. *International Journal of Technology*, Volume 13(6), pp. 1336–1343

Tian, W., Dou, L., Jin, Z., Xiao, J., Li, J., 2020. Full-Color Micro-LED Displays with Cadmium-Free Quantum Dots Patterned by Photolithography Technology. *Applied Optics*, Volume 59(35), pp. 11112–11122

Tuyet, D.T., Quan, V.T.H., Bondzior, B., Dereń, P. J., Velpula, R.T., Nguyen, H.P.T., Tuyen, L.A., Hung, N.Q., Nguyen, H.D., 2020. Deep Red Fluoride Dots-In-Nanoparticles for High Color Quality Micro White Light-Emitting Diodes. *Optics Express*, Volume 28(18), pp. 26189–26199

Wang, W., Cheng, C., Wang, H., Lin, G., 2020. White-Light Color Conversion With Red/Green/Violet Laser Diodes and Yellow Light-Emitting Diode Mixing for 34.8 Gbit/s Visible Lighting Communication. *Photonics Research*, Volume 8(8), pp. 1398–1408

Yu, X., Xiang, L., Zhou, S., Pei, N., Luo, X., 2021. Effect of Refractive Index of Packaging Materials on The Light Extraction Efficiency of COB-LEDs with Millilens Array. *Applied Optics*, Volume 60(2), pp. 306–311

Yuce, H., Guner, T., Balci, S., Demir, M.M., 2019. Phosphor-Based White LED by Various Glassy Particles: Control over Luminous Efficiency. *Optics Letter*, Volume 44(3), pp. 479–482

Zhang, C., Yang, B., Chen, J., Wang, D., Zhang, Y., Li, S., Dai, X., Zhang, S., Lu, M., 2020. All-Inorganic Silicon White Light-Emitting Device with An External Quantum Efficiency of 1.0%. *Optics Express*, Volume 28(1), pp. 194–204

Zhang, K., Lu, H.B., Shao, L., Zheng, C., Zhang, Y.J., Huang, S.Y., 2021. Experimental Research on Ammonia Concentration Detection with White Light-Emitting Diodes. *Journal of Optical Technology*, Volume 88(9), pp. 548–552